Check for updates

Liquid phase selective oxidation of veratryl alcohol to veratraldehyde using pure and Mg-doped copper chromite catalysts

S. Jagadeesan,[a] V. Prathipa,[b] C. Ragupathi,[c] G. Ramalingam,[d] S. Narayanan,[c] P. Tamizhdurai, [ID] *[e] A. Rajendran,[f] Krishna Kumar Yadav, [ID] [gh] Ghadah Shukri Albakri,[i] Mohamed Abbas[j] and Maha Awjan Alreshidi[k]

Mg-doped copper chromite ($CuCr_2O_4$) nanocomposites were synthesised through conventional technique. The pure and doped $CuCr_{2-x}Mg_x O_4$ ($x = 0.00–0.1, 0.2$ and 0.3%) nanocomposites were characterized in terms of their morphology, crystal structure, surface area and catalytic performance. The chemical composition of $CuCr_{2-x}Mg_x O_4$ was confirmed *via* FT-IR. The formation of pure and doped catalysts was validated by XRD results. TEM/SEM confirmed the formation of $CuCr_{2-x}Mg_xO_4$ nanoparticles. Mg-doped samples possess a high specific surface area compared to pure $CuCr_2O_4$. Thus, the effects of temperature, solvent, time, oxidant and the amount of catalyst on the oxidation of veratryl alcohol were reported. Furthermore, detailed mechanisms of the catalytic oxidation of veratryl alcohol as well as the reusability and stability of the nanomaterial were investigated. The resulting composites were shown to be effective heterogeneous catalysts for the oxidation of veratryl alcohol.

1. Introduction

In the field of heterogeneous catalysis, sunlight-activated materials are necessary. Because nanotechnology enables control over their size and morphology, there is a correlation between their increased efficiency and these developments. In the field of catalysis, ternary metal oxides with a spinel structure (AB_2O_4) have demonstrated exceptional properties. Thus, metal oxides were located around the octahedral (B site) and tetrahedral (A site) positions, and the quantities, type of oxides and the location of metal cations in the crystalline structure significantly affect the chemical–physical properties of chromite materials.[1,2] At present, chromite materials with spinel structures are present with a face-centered lattice with the space group $Fd3m$, whereas Cr^{3+} cations are in octahedral positions and Cu^{2+} cations occupy tetrahedral positions.[3] Chromium-based catalysts exhibit good resistance to atmospheric effects, high thermal stability, optical properties, resistance to chemical corrosion, photocatalysis, catalysis *etc.* Beyond that, it is interesting to see numerous applications for ceramic materials.[4] The doping of divalent Mg^{2+} metal ions is primarily incorporated into A-site cations in the synthesized copper chromite materials. The stoichiometry of chemical compositions and the controlled crystallite size of chromite materials prepared via the chemical method were found to be extremely favorable for achieving good-quality products.[5] Copper chromates were synthesized using various methods, such as sol–gel, ceramic,[6] microwave and co-precipitation techniques.[7] New chemical methods, such as hydrothermal, sol–gel/citrate,[8] conventional (low-temperature method), and low-temperature solution synthesis methods, were also developed.[9]

[a] Department of Physics, Srimad Andavan Arts and Science College (Autonomous) (Affiliated to Bharathidasan University, Tiruchirappalli), Tiruchirappalli-620005, Tamilnadu, India

[b] Department of Chemistry, PSNA College of Engineering Technology, Dindigul, Tamilnadu, India

[c] Department of Chemistry, Sriram College of Arts and Science, Perumalpattu, Tiruvallur 602024, Tamilnadu, India

[d] Department of Nanoscience and Technology, Alagappa University, Karaikudi 630003, India

[e] Department of Chemistry, Dwaraka Doss Goverdhan Doss Vaishnav College (Autonomous) (Affiliated to the University of Madras), India. E-mail: tamizhvkt2010@gmail.com; Tel: +91-9677146579

[f] Department of Chemistry, Sir Theagaraya College, (Affiliated to University of Madras), Chennai 600 021, Tamilnadu, India

[g] Faculty of Science and Technology, Madhyanchal Professional University, Ratibad, Bhopal, 462044, India

[h] Environmental and Atmospheric Sciences Research Group, Scientific Research Center, Al-Ayen University, Thi-Qar, Nasiriyah, 64001, Iraq

[i] Department of Teaching and Learning, College of Education and Human Development, Princess Nourah Bint Abdulrahman University, P. O. Box 84428, Riyadh 11671, Saudi Arabia

[j] Electrical Engineering Department, College of Engineering, King Khalid University, Abha 61421, Saudi Arabia

[k] Department of Chemistry, University of Ha'il, Ha'il 81441, Saudi Arabia

Table 1 Sample code and sample composition with their abbreviations

Sample code	Sample composition
a	$CuCr_2O_4$
b	Mg (0.1%) $CuCr_2O_4$
c	Mg (0.2%) $CuCr_2O_4$
d	Mg (0.3%) $CuCr_2O_4$

Mg^{2+} doped chromite based catalysts were used in the selective oxidation reaction. Also, chromite based materials were more useful in industrial and technological applications.[10] Selective oxidation of veratryl alcohol to carbonyl compounds (aldehyde to acid) is highly challenging.[11] Selective oxidation of veratryl alcohol is employed to produce several industrially valuable chemicals, such as those associated with the food and fragrance industries; veratraldehyde is a highly valued chemical that is derived from crude oil and via the methylation of vanillin. It is interesting to note that the industry that utilizes veratraldehyde spends as much as 100 times more on bio-based veratraldehyde than on crude oil-based veratraldehyde.[12–14] Herein, we synthesized citrate $CuCr_2O_4$ and Mg-doped $CuCr_2O_4$ via a conventional combustion route, followed by their morphological and structural characterisation. The chemical–physical properties of the catalysts are characterised using multiple techniques. The resulting composites were shown to be effective heterogeneous catalysts for the oxidation of veratryl alcohol.

2. Experimental

At present, ($CuCr_2O_4$) copper chromite spinel oxides were (flow chart 1) prepared via the conventional combustion route. The following chemicals, such as citric acid $C_6H_8O_7$ (used as fuel), chromium nitrate Cr $(NO_3)_3 \cdot 9H_2O$, copper nitrate Cu $(NO_3)_2 \cdot 6H_2O$ and magnesium nitrate Mg $(NO_3)_2 \cdot 6H_2O$ were used without purification. First stage (I): chromium nitrate 1 M solution and copper nitrate 0.5 M solution were prepared separately in 25 mL (DI) deionized water. Second stage (II): Cr and Cu solutions were mixed and stirred continuously for 1 h to obtain a homogenous solution. Third stage (III): An aqueous solution of 5 M citric acid was prepared in DI water, and the citrate to nitrate ratio was fixed at one. Then, the obtained solution (citrate) is dropped into the nitrate solution under continuous stirring, and the homogeneous solution is neutralized with the addition of ammonium hydroxide (NH_4OH). Following this, different amounts (0.1%, 0.2%, and 0.3%) of magnesium nitrate hexahydrate (0.3 M) were introduced into the aforementioned solution. Fourth stage (IV): the overall homogenous solution was evaporated using a heating system; it was kept on a hot plate at 100 °C with intensive stirring for about 1–2 hours. Thus, a highly viscous gel was obtained. Fifth

stage (V): the extremely viscous gel was then transferred to a muffle furnace, where self-ignition was initiated at an experimental temperature of 400 °C/5 hours. The samples (Table 1) of the (0.0) undoped $CuCr_2O_4$ and (0.1 to 0.3) from Mg-doped $CuCr_2O_4$ were labelled (a) and (b) to (d).

2.1. Instrumental

X-ray diffraction analysis was carried out using a Rigaku DMAX-3A powder diffractometer with CuKα radiation at a wavelength of 1.54 Å to investigate the crystalline phase and the various structural parameters of the prepared samples. These patterns of XRD were scanned in a 2θ range of 20° to 80° with a scanning step size of 0.05°. The morphology was characterized via field-emission scanning electron microscopy (FESEM) (SEM, QUANTA FEG 250, USA) and transmission electron microscopy (TEM). The specific surface areas (BET) of the products were tested using a Micromeritics ASAP 2020 apparatus. Fourier-transform infrared (FTIR) spectra were recorded using a thermo scientific Nicolet iS10 instrument in an in situ Harrick IR cell.

2.2. Catalytic test

Catalytic oxidation of alcohol was carried out on a batch reactor functioning under atmospheric conditions. 10 mmol of (CH_3CN, DMF and $CHCl_3$), 10 mmol of veratryl alcohol (at a molar ratio of H_2O_2/alcohol of 1 : 1), and 10 mmol of oxidant (TBHP/H_2O_2) was added along with 0.1 to 0.3 g of the pure and Mg-doped copper chromites, and the fillings were heated to 100 °C at different reaction times for 12 h at altered time intervals in a three-necked round bottom flask equipped with a reflux condenser and the thermometer.
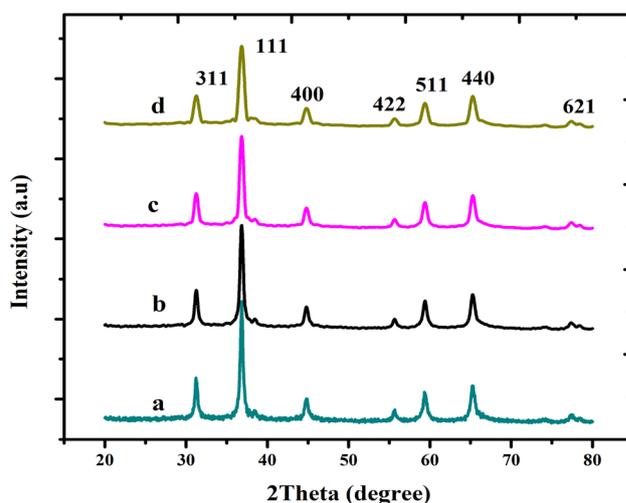

Fig. 1 X-ray diffraction pattern of (a) $CuCr_2O_4$ and (b–d) Mg-doped $CuCr_2O_4$.

Chromium nitrate 1 M solution, and copper nitrate 0.5M solution

Dissolved 25 ml (DI) deionized water/1.hrs.
(Stirring continuously)

Together (Cr and Cu) get the homogenous solution + citrate towards nitrate ratio were fixed on the one

Homogeneous solution is reached on the for addition (NH₄OH)

Magnesium nitrate hexahydrate, 0.3 M dopant concentration (0.1%, 0.2% and 0.3%)

Overall homogenous solution /heating system on the 100°C by stirring form about 1-2 hours

Highly viscous gel into 400°C/5hours

Pure and Mg doped samples

Flow chart of synthesis form pure and Mg doped copper chromites

From these values, the overall conversion of the reactant veratryl alcohol and the selectivity of the product (3) was estimated.

$$\text{Conversion } (\%) = \frac{V_{\text{veratrylalcohol}} - V_{\text{veratraldehyde}}}{V_{\text{veratrylalcohol}}} \times 100$$

$$\text{Selectivity } (\%) = \frac{V_{\text{veratraldehyde}}}{\text{Consumed}_{\text{veratrylalcohol}}} \times 100,$$

$$\text{Yield} = \frac{\text{moles product produced}}{\text{moles paraffin charged}} \times 100\%$$

3. Results and discussion

3.1. XRD pattern of the Mg-doped CuCr₂O₄ nanocomposites

The XRD measurements were performed to determine the effectiveness of the production on the pure and Mg-doped CuCr₂O₄. As shown in Fig. 1, the obtained XRD peaks are indexed as undoped and Mg-CuCr₂O₄ with a cubic structure formation. As confirmed by a standard card (JCPDS No. 34-

0424), these XRD peaks conform to undoped and Mg-CuCr₂O₄, matching well with the standard. As the amount of Mg doping increased from $x = 0$ to 0.1, 0.2, and 0.3%, the samples showed only copper chromite's phase, and the peak intensities were comparable with the pure CuCr₂O₄ sample. This indicates the integrity of the Mg dopant within the copper chromite crystal structure. XRD patterns ranging from 35.5° to 37.5° were assigned to the 111 plane, which has the highest intensity. Furthermore, the primary peaks at 2θ-values adhering to the (111) and (311) planes show a small change as the doping concentration of Mg quantity increases. The XRD peaks of the

Table 2 Crystallite size, lattice parameters and lattice strain of copper chromite and Mg-doped copper chromates

Samples	Crystallite size (nm)	Lattice parameters		Strain
		$a = b$ (Å)	c (Å)	
a	43.12	5.9832	3.9810	3.234
b	38.45	5.9833	3.9811	3.091
c	31.45	5.9835	3.9833	2.981
d	29.98	5.9837	3.9835	2.567

samples progressively changed between low and high angles, which correlated with the extension (Table 2) of the lattice parameters, cell volume ($Å^3$) and d spacing values. Thus, ionic radii of Mg^{2+} = 86 pm, Cr^{3+} = 75.5 pm, and Cu^{2+} = 77 pm were compared. Mg-doped copper chromites have smaller crystallite sizes than pure copper chromites due to the substitution of the lattice ions by the Mg^{2+} ions and their entry into interstitial locations.[15,16]

The average crystallite size was determined using the Scherrer formula:[17]

$$L = \frac{0.89\lambda}{\beta \cos\theta},$$

where L is the mean crystal size (Å) and λ is the wavelength of the X-ray source (1.5404 Å), thus, in the XRD pattern, θ and β correspond to the (radians) diffraction angle of the observed peaks and the full width at half maximum (FWHM), respectively. 0.89 is the Scherrer constant. Thus, for peak position, FWHM can be acquired with two Gaussian curves by fitting the measured peaks. The monochromatic Cu Kα radiation was used a X-ray source. Based on the results of X-ray diffraction, the decrease in crystallite size from (a) pure $CuCr_2O_4$ 43.12 nm, Mg-doped $CuCr_2O_4$ samples (b–d) 38.45 nm, 31.45 to 29.98 nm could be linked to maximizing the concentrations of dopant.

3.2. FTIR spectra

Fourier transform infrared (FTIR) spectroscopy was recorded for the four undoped samples (Fig. 2a and b) and Mg-CuCr$_2$O$_4$ around room temperature from 400 to 4000 cm^{-1}. Thus, two sharp bands for the different absorption peaks observed around 561 and 475 cm^{-1} lower frequency band (ν_2) correspond to the vibration of $–Mg^{2+}–Cr^{3+}–O^{2+}$ by sites, indicating the formation of octahedrons and tetrahedrons, respectively (Table 3). The bands around 560–470 cm^{-1} correspond to the intrinsic stretching vibration of metal ions at the tetrahedral site, and the band in the range of 510–550 cm^{-1} is attributed to the M–Mg–O

Table 3 FTIR modes (ν_1 and ν_2) of copper chromite and Mg-doped copper chromite

Samples	Wave number ν_1 (cm^{-1})	Wave number ν_2 (cm^{-1})
a	613, 801	898, 1125
b	608, 799	894, 1122
C	605, 796	890, 1120
D	661, 856	1118

bond vibration. These two bands positioned a high-frequency band (ν_1) at 500 and 678 cm^{-1} characteristic of $CuCr_2O_4$ spinel. The FT-IR spectra exhibited two characteristic absorption bands at 600 and 900 cm^{-1}, corresponding to the tetrahedral and octahedral formations, respectively. Thus, both bands similarly correspond to the asymmetric stretching vibrations of Cr–O–Cu–Mg. In general, Mg substitution *via* transition metal ions, such as Cu^{2+}, leads to a shift in the frequency bands and is due to the variation of CrO_4 bond length.[18,19]

3.3. Morphology

SEM images and micrographs of the undoped and Mg-CuCr$_2$O$_4$ compositions (x = 0.00, 0.1, 0.02 and 0.03%) are demonstrated in Fig. 3a–d. The SEM images and micrographs show irregularly shaped large grains of undoped and smaller grains of Mg-CuCr$_2$O$_4$. In the arrangement within the SEM results, the samples have an extensive particle distribution and present strong agglomerations; hence, a measurement from the particle size was not possible. However, the obtained results give some statistical arrangements of Mg–Cu–Cr–O. As can be observed, SEM images detect particularly pure and doped sample differences between XRD crystallite sizes and particle sizes, as shown in Table 4. The crystallite size determined using the XRD approach was found to be correct, however the grain size assessed using the SEM analysis had broader values and may
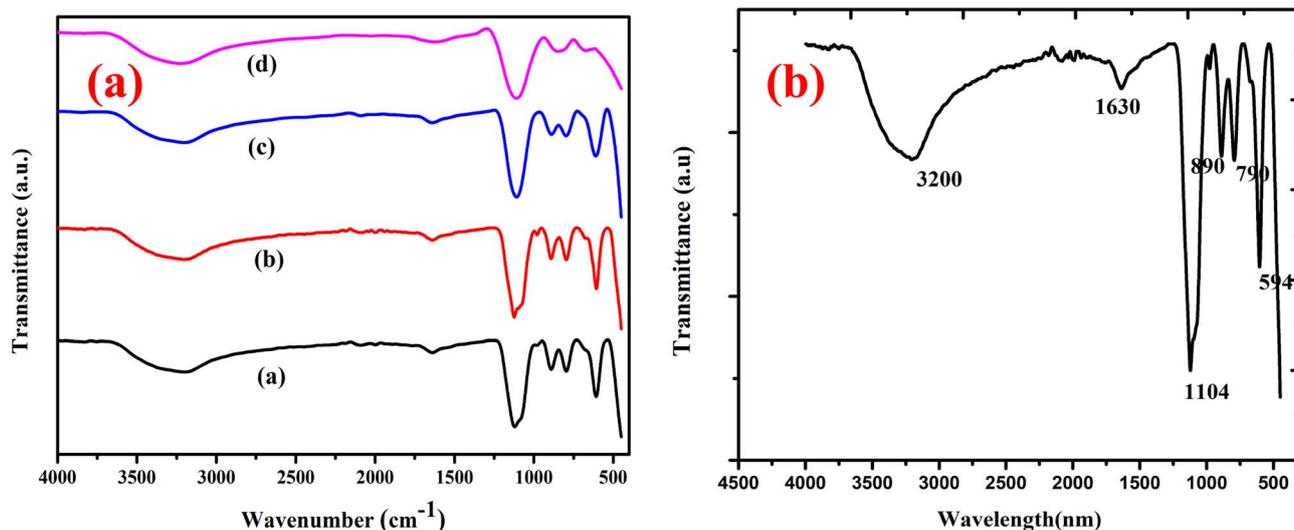

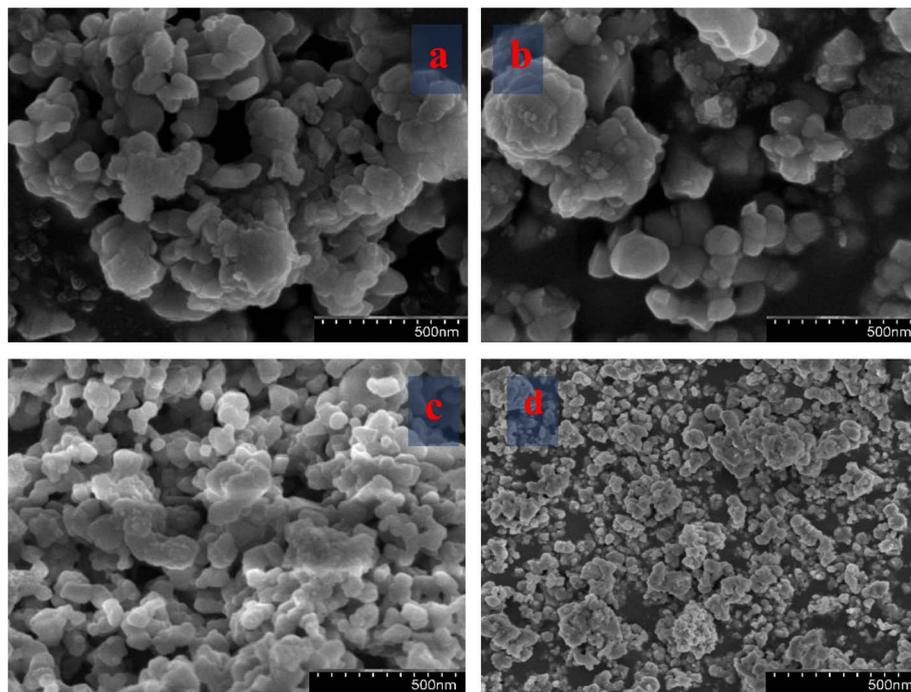**Fig. 2** (a) FTIR spectra of (a) CuCr$_2$O$_4$ and (b–d) Mg-doped CuCr$_2$O$_4$; (b) FTIR spectra of pure CuCr$_2$O$_4$.

Fig. 3 SEM showing (a) $CuCr_2O_4$ and (b–d) Mg-doped $CuCr_2O_4$.

Table 4 Difference between the calculated crystallite sizes (XRD) of samples and the grain sizes (SEM) of copper chromite and Mg-doped copper chromites

Samples	Crystallite size from XRD (nm)	Particle size from SEM (nm)
a	43.12	49–53
b	38.45	43–39
c	31.45	40–31
D	29.98	39–29

have measurement errors. In our studies, $CuCr_2O_4$ nanocomposites having a cluster-like structure with sizes ranging from 100 to 500 nm made by identical particles. Pure and doped samples both have discrete particle-like appropriate interfaces in $CuCr_2O_4$ nanocomposites. In addition, it is noticed that the structure can be obtained at lower synthesis temperatures from the conventional method.[20] Thus, TEM was used to control the morphologies and particle size of copper chromite and the Mn doping copper chromite. As illustrated in Fig. 4a–d, spherical particles and regular structures are present in the doped samples. TEM images for $CuCr_2O_4$ particles were obtained and the particle-like shape changed to form spherical particles, as concentration on the Mg^{2+} is improved.

3.4. Surface area analysis

Thus, a specific surface area can be used from the BET equation to determine the amount of nitrogen absorbed into copper chromite and the Mn doping copper chromite. The H–K method was used to obtain the average pore diameter, and the *t*-

plot method was employed to obtain the total pore volume. In terms of catalytic activity, surface area is an important parameter when evaluating potential catalytic applications involving catalytic materials such as copper chromite and Mg-doped copper chromite. Table 5 displays the pore volume (V_p), specific surface area (S_{BET}), pore radius (R_p), and crystallite size (nm). The copper chromite and Mg-doped copper chromite samples increase the surface area for converted catalytic applications because they demonstrate increasing contact between alcohol reacting molecules and aldehyde from the active sites.[21,22] For all the samples, this was followed by the type III isotherms with the hysteresis loop at the high P/P_0 and illuminating the representative mesoporous material.[23] The system, copper chromite and the Mg-doped copper chromite of the plot on the amount of gas adsorbed as a function of the relative pressure are exposed altogether as a type-III (a–d) and with hysteresis loop, as shown in Fig. 5a.

When magnesium is added, the bulk copper chromite phase grows more slowly, increasing the surface area, improving porosity, and creating micropores. Because of nonisomorphic substitution, the addition of magnesium to the copper chromite phase matrix causes a decrease in grain size, which results in an increase in surface area. The three components of Mg, Cr, and Cu can form pores in their matrices, leading to the production of pores of varying sizes. The reduction in grain size and the non-isomorphic substitution of Mg in the copper chromite matrix resulted in the formation of significant micropores, which is why the average pore diameter for the Mg-doped sample decreased. Thus, the addition of Mg, which simultaneously increases the mesopores and introduces micropores, increases the catalytic activity of copper chromites.[24,25]
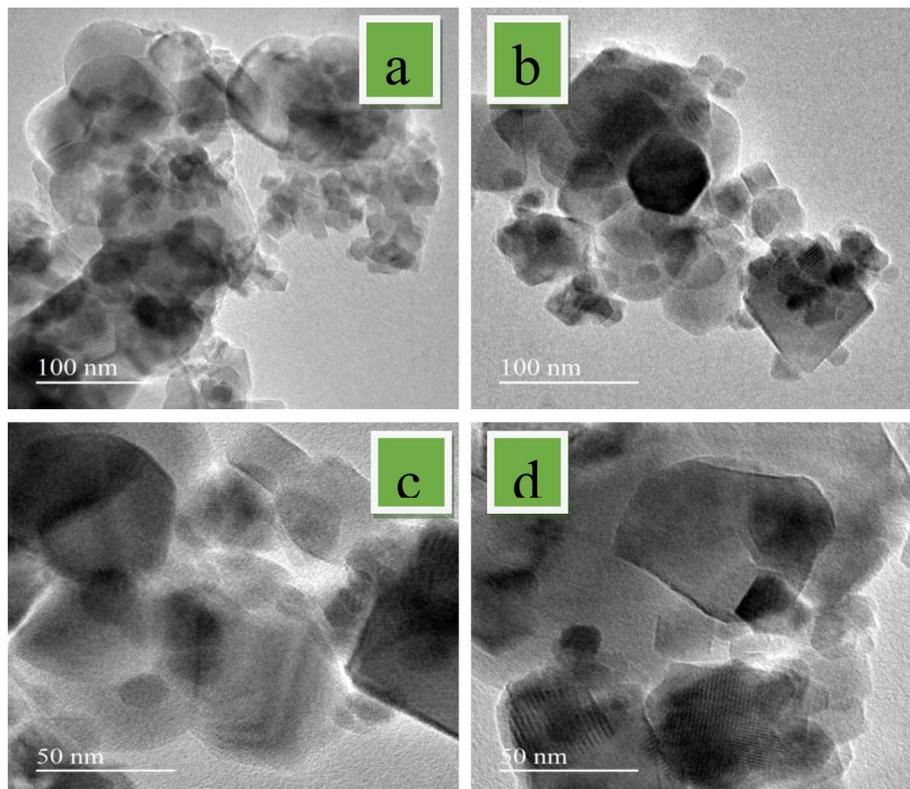
Fig. 4 TEM images of (a) $CuCr_2O_4$ and (b–d) Mg-doped $CuCr_2O_4$.

Table 5 BET surface area, average pore diameter, pore volume and crystallite size (nm) of $CuCr_2O_4$ and Mg-doped $CuCr_2O_4$

Parameters	a	b	c	d
S_{BET} ($m^2\ g^{-1}$)	38.2	40.2	57.8	63.4
S_{mic} ($m^2\ g^{-1}$)	2.9	5.1	7.5	9.2
S_{meso} ($m^2\ g^{-1}$)	35.3	35.1	50.0	54.1
Total pore volume ($cm^3\ g^{-1}$)	0.1	0.1	0.1	0.2
Micro pore volume ($cm^3\ g^{-1}$)	0.0	0.0	0.1	0.1
Meso pore volume ($cm^3\ g^{-1}$)	0.1	0.1	0.0	0.1
Average pore diameter (nm)	13.6	14.1	17.9	19.8

4. Catalytic activity of selective oxidation

4.1. Effect of temperatures

The effect of temperature on selectivity towards veratryl aldehyde and the conversion of veratryl alcohol were studied in the range of 60–140 °C, as presented in Fig. 6. The selectivity (80%) of veratryl aldehyde decreases with increasing temperature, which is particularly due to the over-oxidation of veratryl aldehyde to veratric acid. However, conversion of veratryl alcohol increased from 60 to 80% with an increase in the temperature from 60 to 140 °C.[26–28] This system increased the reaction temperature, which was important for the decrease in the oxygen, resulting in unfavorable product formation. The optimum temperature is 100 °C.

4.2. Amount of catalyst

The effect of catalyst amount (0.1 g to 0.5 g) on the selectivity of veratryl aldehyde and the conversion of veratryl alcohol into by-products formation were studied and the results are presented in Fig. 7. The catalytic activity is closely related to the following two factors: the copper chromite amount of catalyst for the active sites Cu and Cr and the size for O^{2-}. The doping concentration of Mg was determined to ensure appropriate active Mg sites; however, smaller Mg particles are usually obtained. Therefore, the optimal pure and doping copper chromites are 0.3 g because they give the best yield among others. However, the amount of catalyst interaction with the catalyst regenerates the catalyst surface, causing the product molecules to desorb and encouraging additional oxidation.

4.3. Effect of reaction time

This conversion of veratryl alcohol and the selective formation of product are observed at different reaction time intervals of 0.5, 1, 2, 4, 6, 8, 10, 12 and 14 h. As demonstrated in Fig. 8, 11% veratryl alcohol conversion and 50% veratryl aldehyde selectivity are obtained at 0.5 h; after allowing the reaction for 10 h, 80% yields were formed. The main product was veratryl aldehyde with veratryl acid as a by-product. Based on the catalytic reaction route, to increase the conversion of aldehyde, the reaction time needs to be prolonged. Thus, the catalytic activity was achieved with a reaction time of 12 h and a high yield was obtained, and the time was increased as the products formed.[29] Thus, an optimum catalytic reaction time of 12 h was selected.
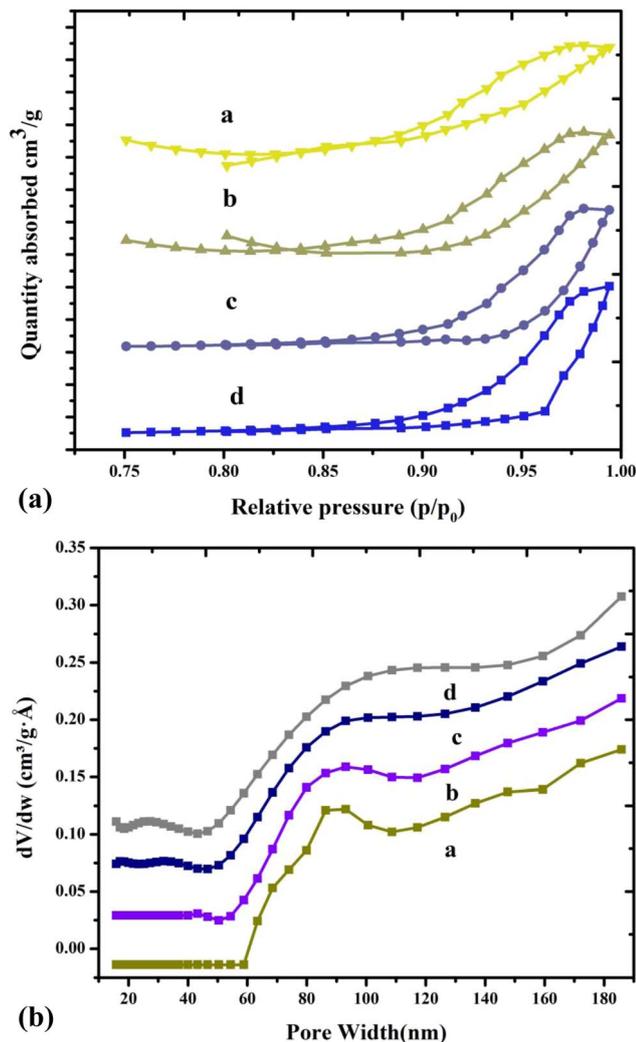
Fig. 5 (a) N$_2$ adsorption/desorption isotherms of (a) pure and (b–d) Mg-doped copper chromite. (b) Pore size distributions of (a) pure and (b–d) Mg-doped copper chromites.

Fig. 6 Catalytic activity of the catalysts *versus* different reaction temperatures in the oxidation of veratryl alcohol. Reaction conditions: pure and doped samples: 0.3 g; alcohol: 10 mmol; acetonitrile: 10 mmol; H$_2$O$_2$: 10 mmol; time: 12 h; temperature: 60 to 140 °C.

Fig. 7 Yield of the product *via* the selective oxidation of veratryl alcohol using different catalysts. Reaction conditions: pure and doped samples: 0.1 to 0.5 g; alcohol: 10 mmol; acetonitrile: 10 mmol; H$_2$O$_2$: 10 mmol; time: 12 h; temperature: 100 °C.

4.4. Effect of solvents

The catalytic performance was evaluated in several solvents, such as chloroform (CHCl$_3$), acetonitrile (CH$_3$CN) and dimethyl formamide (DMF), for the conversion of veratryl alcohol to veratryl aldehyde. Thus, a solvent plays an important role in the reaction induced by the alcohol conversion of an aldehyde decomposed for the by-products. Consequently, a higher yield for acetonitrile than for dimethyl formamide and chloroform was observed, as listed in Table 6. For this reason, a polar solvent was more easily adsorbed on the catalyst surface, preventing the adsorption of alcohol to aldehyde. Because the substrates and oxidants are more soluble in the solvent, they can more readily bind to the catalyst's active sites. Therefore, acetonitrile was the more active solvent for the catalytic system under study. In the case of CHCl$_3$ and DMF, the yields are lower compared to acetonitrile, might be due to the inefficient hydrogen transfer by solvents, and the incomplete solubility of organic substrates and catalytic systems in the solvents. It turned o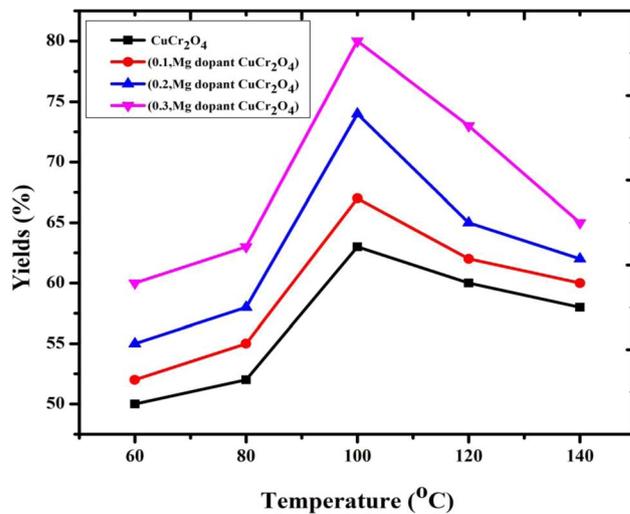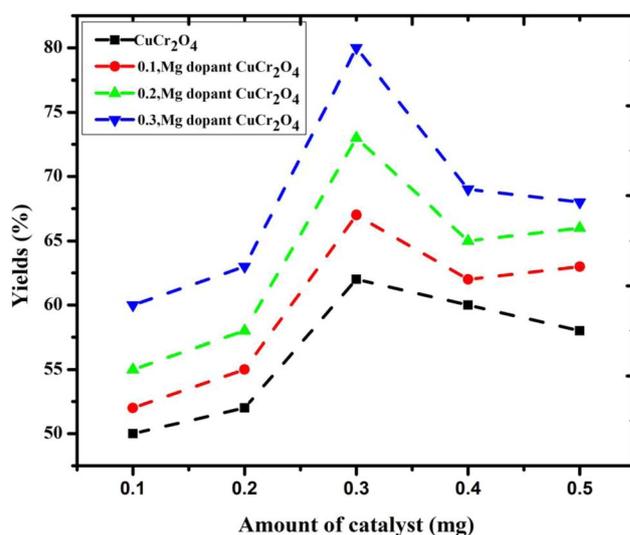ut that the conversion of alcohol depended on the polarity of the solvent molecules, polarity order from acetonitrile, dimethyl formamide and chloroform. Besides, acetonitrile was selected as the solvent for the catalytic system.

4.5. Effect of oxidants

Catalytic performance for oxidation as a function of the oxidant played an important role. This catalytic reaction is controlled by the option for the reaction to occur due to the contribution of the oxygen lattice (Fig. 9) from the oxidant. Hereafter, the reaction was successively carried out in the presence of different oxidants, such as TBHP and hydrogen peroxide. TBHP was slightly soluble on the selected organic substrate and the
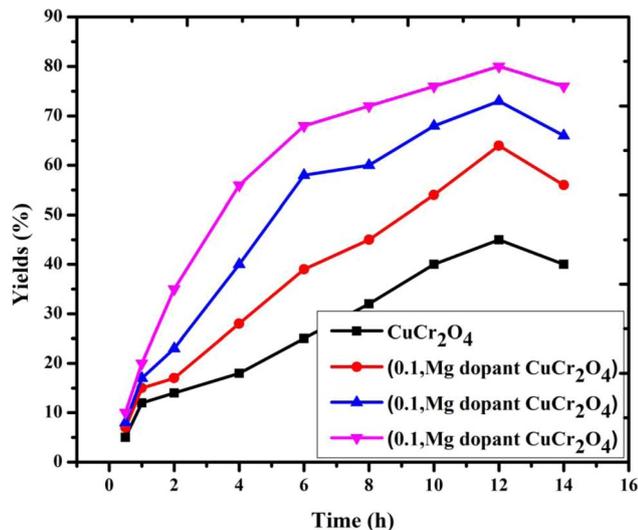
Fig. 8 Catalytic activity of the catalysts *versus* different reaction times for the selective oxidation of veratryl alcohol. Reaction conditions: pure and doped samples: 0.3 g; alcohol: 10 mmol; acetonitrile: 10 mmol; H_2O_2: 10 mmol; time: 0 to 16 h; temperature: 100 °C.

Table 6 Yield of the product in different oxidants obtained *via* veratryl alcohol[a]

Samples	Chloroform	Dimethyl formamide	Acetonitrile
a	32	40	46
b	45	54	65
c	59	67	78
d	68	73	83

[a] Reaction conditions: pure and doped samples: 0.3 g; alcohol: 10 mmol; acetonitrile: $CHCl_3$ and DMF 10 mmol; H_2O_2: 10 mmol; time 12 h: temperature: 100 °C.

catalytic system. As a result, the yield of veratryl aldehyde is low in all synthesized $CuCr_2O_4$ nanomaterials. In the case of H_2O_2, the solubility on the chosen organic substrate could be higher. In conclusion, H_2O_2 on acetonitrile was usual because the establishment of the peroxycarboximidic acid was intermediate and the transfer agent was good oxygen. Hence, the choice of the oxidant was hydrogen peroxide.[30,31]

4.6. Mechanism

A proposed mechanism in Scheme 1 suggests that H_2O_2 molecules undergo homolytic cleavage, resulting in two hydroperoxy radicals. These radicals react with Cr^{3+} and Cu^{2+} ions on the surface of $CuCr_2O_4$, creating Cr^{2+} and Cu^+ ions and regenerating hydroperoxyl. The hydroperoxy radicals also react with hydroxy radicals on the surface to form water and oxygen. Veratryl alcohol molecules are adsorbed onto the surface of $CuCr_2O_4$, forming metal-alkoxide intermediates and adsorbing hydrogen *via* O–H bond cleavage. The surface O–H group is formed by bonding adsorbed hydrogen with the surface lattice oxygen and coordinating with the carbon atom of the methyl group in the veratryl alcohol molecule. Finally, the C–H bond in the
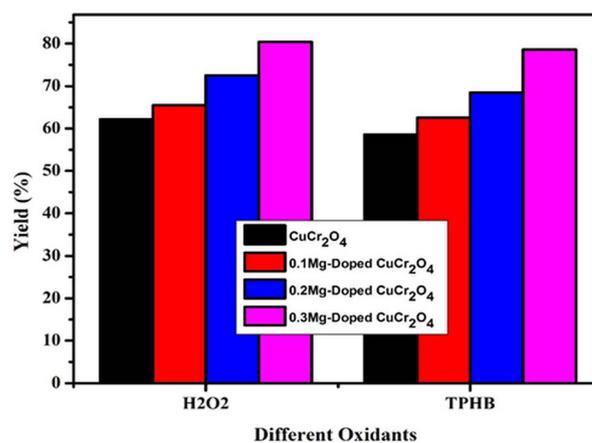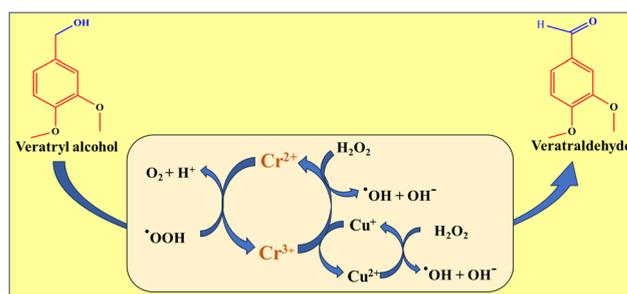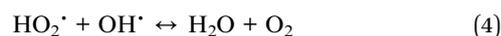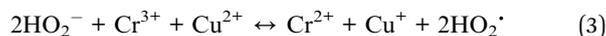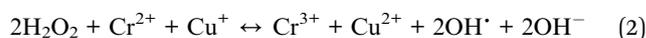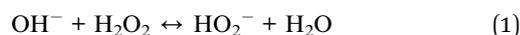

Fig. 9 Effect of oxidants in the selective oxidation of veratryl alcohol. Reaction conditions: pure and doped samples: 0.3 g; alcohol: 10 mmol; acetonitrile: 10 mmol; TBHP and H_2O_2: 10 mmol; time: 12 h; temperature: 100 °C.

Scheme 1 Shows the selective oxidation of veratryl alcohol to veratraldehyde.

β position is activated, resulting in the formation of veratraldehyde and water. The oxygen adsorbed onto the support surface dissociates into chemisorbed oxygen species and diffuses into the lattice vacancies of the support. This is followed by activation in the oxygen vacancies and conversion into lattice oxygen (O^{2-}). The lattice oxygen further transfers to the surface of $CuCr_2O_4$ through oxygen-deficient sites, restoring the interface between the $CuCr_2O_4$ active sites.[32–35]

$$OH^- + H_2O_2 \leftrightarrow HO_2^- + H_2O \tag{1}$$

$$2H_2O_2 + Cr^{2+} + Cu^+ \leftrightarrow Cr^{3+} + Cu^{2+} + 2OH^{\bullet} + 2OH^- \tag{2}$$

$$2HO_2^- + Cr^{3+} + Cu^{2+} \leftrightarrow Cr^{2+} + Cu^+ + 2HO_2^{\bullet} \tag{3}$$

$$HO_2^{\bullet} + OH^{\bullet} \leftrightarrow H_2O + O_2 \tag{4}$$

4.7. Recyclability of the catalyst

To examine the recyclability of the catalyst, the oxidation of veratryl alcohol to veratraldehyde was repeated five times with the same catalyst. The percentage conversion of veratraldehyde slightly decreased. The catalysts after the reaction were recovered by centrifugation, washed with ethanol, and then dried and
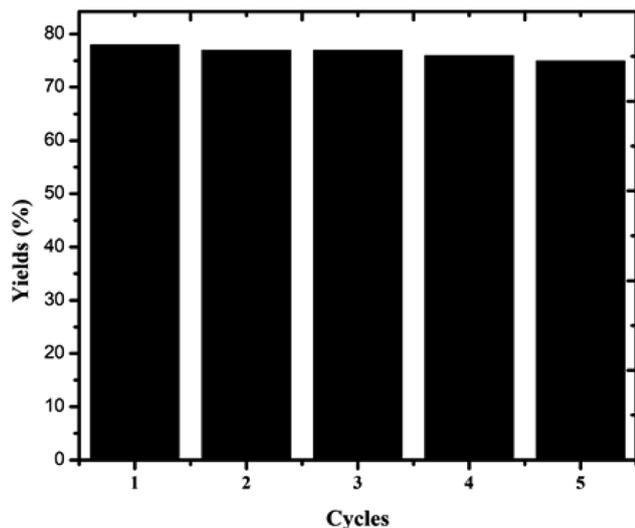
Fig. 10 Cycling performance of the copper chromite catalysts.

reused for another reaction under the same conditions, as shown in Fig. 10. From this determination, the samples were filtered and the residue was washed several times with acetone and dried at 120 °C in an air oven for 3 h; this was repeated five times under identical catalytic conditions. Consequently, considering the small amount of catalyst used in the reaction, the great loss of catalyst should be due to the process of washing, which could be easily addressed in the large scale industrial production.

During the catalytic oxidation of veratryl alcohol to veratraldehyde, O–H bonds are broken and attended through the formation of hydrogen atoms, which further react with oxygen to generate water to achieve dehydrogenation to produce veratraldehyde. Subsequently, one hydrogen atom in the CHO groups was formed *via* a broken O–H bond, forming a metal–alcohol salt intermediate. Further, the objectivity of the hydrogen atom from carbon induces the conversion of the alcohol group into an aldehyde.

5. Conclusions

This paper demonstrates a simple method for producing efficient catalysts for the catalytic oxidation of veratryl alcohol to veratraldehyde. The further detachment of a hydrogen atom from carbon causes the alcohol group to be converted into an aldehyde group, resulting in the creation of an intermediate and veratric acid. XRD confirmed the development of the spinel phase. Thus, pure and Mg-doped spinels were found to be highly porous, as confirmed by SEM. Thus, copper chromite nanocomposites with a crystallite size in the range of 43–29 nm were synthesized. FT-IR was used to confirm the formation of the spinel phase. The current technology is applicable to various d and f block metal-supported catalysts for further catalytic processes.

Conflicts of interest

There are no conflicts to declare.

References

1 V. K. Gupta, N. Atar, M. L. Yola, Z. Üstündağ and L. Uzun, A novel magnetic Fe@Au core-shell nanoparticles anchored grapheneoxide recyclable nanocatalyst for the reduction of nitrophenolcompounds, *Water Res.*, 2014, **48**, 210–217.

2 R. Saravanan, M. M. Khan, V. K. Gupta, E. Mosquera, F. Gracia, V. Narayanan and A. Stephen, ZnO/Ag/Mn2O3nanocomposite for visible light-induced industrial textile effluent degradation, uric acid and ascorbic acid sensing and antimicrobial activity, *RSC Adv.*, 2015, **5**, 34645–34651.

3 V. K. Gupta, I. Ali, T. A. Saleh, M. N. Siddiqui and S. Agarwal, Chromium removal from water by activated carbon developed from waste rubber tires, *Environ. Sci. Pollut. Res.*, 2013, **20**, 1261–1268; S. Sessarego, S. C. G. Rodrigues, Y. Xiao, Q. Lu and J. M. Hill, Phosphonium-enhanced chitosan for Cr(VI) adsorption in waste water treatment, *Carbohydr. Polym.*, 2019, **211**, 249–256.

4 R. J. Bartlett, Chromium cycling in soils and water: Links, gaps, and methods, *Environ. Health Perspect.*, 1991, **92**, 17–24.

5 G. Chen, C. Qiao, Y. Wang and J. Yao, Synthesis of magnetic gelatin and its adsorption property for Cr(VI), *Ind. Eng. Chem. Res.*, 2014, **53**, 15576–15581.

6 B. Qiu, H. Gu, X. Yan, J. Guo, Y. Wang, D. Sun, Q. Wang, M. Khan, X. Zhang, B. L. Weeks, D. P. Young, Z. Guo and S. Wei, Cellulose derived magnetic mesoporous carbon nanocomposites with enhanced hexavalent chromium removal, *J. Mater. Chem. A*, 2014, **2**, 17454–17462.

7 S. S. Banerjee, M. V. Joshi and R. V. Jayaram, Removal of Cr(VI)and Hg(II) from aqueous solutions using fly ash and impregnated flyash, *Sep. Sci. Technol.*, 2005, **39**, 1611–1629.

8 W. Jiang, Q. Cai, W. Xu, M. Yang, Y. Cai, D. D. Dionysiou and K. E. O'Shea, Cr(VI) adsorption and reduction by humic acid coated on magnetite, *Environ. Sci. Technol.*, 2014, **48**, 8078–8085.

9 J. Zhao, Z. Li, J. Wang, Q. Li and X. Wang, Capsular polypyrrolehollow nanofibers: an efficient recyclable adsorbent for hexavalentchromium removal, *J. Mater. Chem. A*, 2015, **3**, 15124–15132.

10 Y. Liu, L. Song, L. Du, P. Gao, N. Liang, S. Wu, T. Minami, L. Zang, C. Yu and X. Xu, Preparationofpolyaniline/emulsionmicrosphere composite for efficient adsorption of organic dyes, *Polymers*, 2020, **12**, 167.

11 N. Ballav, H. J. Choi, S. B. Mishra and A. Maity, Polypyrrole-coatedhalloysite nanotube clay nanocomposite: synthesis,

characterization and Cr(VI) adsorption behaviour, *Appl. Clay Sci.*, 2014, **102**, 60–70.

12 J. Wang, Y. Wen, X. Feng, Y. Song and L. Jiang, Control over the wettability of colloidal crystal films by assembly temperature, *Macromol. Rapid Commun.*, 2006, **27**, 188–192.

13 A. Rugge, W. T. Ford and S. H. Tolbert, From a colloidal crystal to an interconnected colloidal array: A mechanism for a spontaneous rearrangement, *Langmuir*, 2003, **19**, 7852–7861.

14 J. Tan, Y. Song, X. Huang and L. Zhou, Facile functionalization of natural peach gum polysaccharide with multiple amine groups for highly efficient removal of toxic hexavalent chromium (Cr(VI)) ions from water, *ACS Omega*, 2018, **3**, 17309–17318.

15 M. Bhaumik, A. Maity, V. V. Srinivasu and M. S. Onyango, Removal of hexavalent chromium from aqueous solution usingpolypyrrole-polyaniline nanofibers, *Chem. Eng. J.*, 2012, **181–182**, 323–333.

16 M. Mobarak, E. A. Mohamed, A. Q. Selim, L. Sellaoui, A. B. Lamine, A. Erto, A. Bonilla-Petriciolet and M. K. Seliem, Surfactant−modified serpentine for fluoride and Cr(VI) adsorption in single and binary systems: Experimental studies and theoretical modeling, *Chem. Eng. J.*, 2019, **369**, 333–343.

17 M. N. Hasan, M. S. Salman, A. Islam, H. Znad and M. M. Hasan, Sustainable composite sensor material for optical cadmium(II) monitoring and capturing from wastewater, *Microchem. J.*, 2021, **161**, 105800.

18 K. T. Kubra, M. M. Hasan, M. N. Hasan, M. S. Salman, M. A. Khaleque, M. C. Sheikh, A. I. Rehan, A. I. Rasee, R. M. Waliullah, M. E. Awual, M. S. Hossain, A. K. D. Alsukaibi, H. M. Alshammari and M. R. Awual, The heavy lanthanide of Thulium(III) separation and recovery using specific ligand-based facial composite adsorbent, *Colloids Surf., A*, 2023, **667**, 131415.

19 M. S. Salman, M. N. Hasan, M. M. Hasan, K. T. Kubra, M. C. Sheikh, A. I. Rehan, R. M. Waliullah, A. I. Rasee, M. E. Awual, M. S. Hossain, A. K. D. Alsukaibi, H. M. Alshammari and M. R. Awual, Improving copper(II) ion detection and adsorption from wastewater by the ligand-functionalized composite adsorbent, *J. Mol. Struct.*, 2023, **1282**, 135259.

20 A. Somy, M. R. Mehrnia, H. D. Amrei, A. Ghanizadeh and M. Safari, Adsorption of carbon dioxide using impregnated activated carbon promoted by Zinc, *Int. J. Greenhouse Gas Control*, 2009, **3**, 249–254.

21 A. K. Kercher and D. C. Nagle, Microstructural evolution during charcoal carbonization by X-ray diffraction analysis, *Carbon*, 2003, **41**, 15–27.

22 M. M. Hasan, K. T. Kubra, M. N. Hasan, M. E. Awual, M. S. Salman, M. C. Sheikh, A. I. Rehan, A. I. Rasee, R. M. Waliullah, M. S. Islam, S. Khandaker, A. Islam, M. S. Hossain, A. K. D. Alsukaibi, H. M. Alshammari and M. R. Awual, Sustainable ligand-modified based composite material for the selective and effective cadmium(II) capturing from wastewater, *J. Mol. Liq.*, 2023, **371**, 121125.

23 M. R. Awual, I. M. M. Rahman, T. Yaita, M. A. Khaleque and M. Ferdows, PH dependent Cu(II) and Pd(II) ions detection and removal from aqueous media by an efficient mesoporous adsorbent, *Chem. Eng. J.*, 2014, **236**, 100–109.

24 A. Dandekar, R. T. K. Baker and M. A. Vannice, Characterization of activated carbon, graphitized carbon fibers and synthetic diamond powder using TPD and DRIFTS, *Carbon*, 1998, **36**, 1821–1831.

25 Z. Oruç, M. Ergüt, D. Uzunoğlu and A. Özer, Green synthesis of biomass-derived activated carbon/Fe-Zn bimetallic nanoparticles from lemon (Citrus limon (L.) Burm. f.) wastes for heterogeneous Fenton-like decolorization of Reactive Red 2, *J. Environ. Chem. Eng.*, 2019, **7**, 103231.

26 S. Naghash-Hamed, N. Arsalani and S. B. Mousavi, The Catalytic Reduction of Nitroanilines Using Synthesized $CuFe_2O_4$ Nanoparticles in an Aqueous Medium, *ChemistryOpen*, 2022, **11**, 1–10.

27 S. Naghash-Hamed, N. Arsalani and S. B. Mousavi, Facile copper ferrite/carbon quantum dot magnetic nanocomposite as an effective nanocatalyst for reduction of para-nitroaniline and ortho-nitroaniline, *Nano Futures*, 2022, **6**, 045003.

28 G. I. Danmaliki and T. A. Saleh, Effects of bimetallic Ce/Fe nanoparticles on the desulfurization of thiophenes using activated carbon, *Chem. Eng. J.*, 2017, **307**, 914–927.

29 Y. Hu, G. Jiang, G. Xu and X. Mu, Hydrogenolysis of lignin model compounds into aromatics with bimetallic Ru-Ni supported onto nitrogen-doped activated carbon catalyst, *Mol. Catal.*, 2018, **445**, 316–326.

30 S. Bose, T. Mukherjee and M. Rahaman, Simultaneous adsorption of manganese and fluoride from aqueous solution via bimetal impregnated activated carbon derived from waste tire: Response surface method modeling approach, *Environ. Prog. Sustainable Energy*, 2021, **40**, e13600.

31 M. Pirmoradi, N. Janulaitis, R. J. Gulotty Jr and J. R. Kastner, Bi-Metal-Supported Activated Carbon Monolith Catalysts for Selective Hydrogenation of Furfural, *Ind. Eng. Chem. Res.*, 2020, **59**, 17748–17761.

32 P. Pré, G. Huchet, D. Jeulin, J.-N. Rouzaud, M. Sennour and A. Thorel, A new approach to characterize the nanostructure of activated carbons from mathematical morphology applied to high resolution transmission electron microscopy images, *Carbon*, 2013, **52**, 239–258.

33 P. Veerakumar, V. Veeramani, S.-M. Chen, R. Madhu and S.-B. Liu, Palladium Nanoparticle Incorporated Porous Activated Carbon: Electrochemical Detection of Toxic Metal Ions, *ACS Appl. Mater. Interfaces*, 2016, **8**, 1319–1326.

34 Kong, Y.-Y. Xin, B. Li, X.-F. Zhang, Z.-P. Deng, L. H. Huo and S. Gao, Non-enzymatic $CuCr_2O_4$/GCE amperometric sensor for high sensing and rapid detection of nM level H2O2, *Microchem. J.*, 2023, **194**, 109343.

35 T. Tatarchuk, A. Shyichuk, I. Trawczyńska, I. Yaremiy, A. T. Pędziwiatr, P. Kurzydło, B. F. Bogacz and R. Gargula, Spinel cobalt(II) ferrite-chromites as catalysts for H_2O_2 decomposition: Synthesis, morphology, cation distribution and antistructure model of active centers formation, *Ceram. Int.*, 2020, **46**, 27517–27530.